ORIGINAL PAPER

Macro–Meso Fracture and Instability Behaviors of Hollow-Cylinder Granite Containing Fissures Subjected to Freeze–Thaw–Fatigue Loads

Yu Wang[1] · Zhengyang Song[1] · Tianqiao Mao[2] · Chun Zhu[3]

Abstract

Rock structural deterioration induced by coupled freeze–thaw and stress disturbance are a great concern for jointed rock mass during rock constructions in cold regions. Previous studies focused on fracture evolution of intact rock or flawed rock under freeze–thaw–static loads, but the coupling effect of freeze–thaw and cyclic loads on the pre-flawed hollow-cylinder rock is not well understood. This work investigated the influence of freeze–thaw on rock microstructure change and fatigue mechanical behaviors. Testing results show that rock strength, volumetric strain, and lifetime decrease with increasing F–T number. The stiffness degradation caused by cyclic loads is also impacted by the previous freeze–thaw damage. Additionally, the AE ring count and energy count decrease with the increase of F–T treatment. Large fracture signals are captured for rock that has smaller F–T cycles and at the stress-increasing moment. The AE b-value increases with F–T cycles, and it decreases rapidly near rock failure. Spectral analysis indicates that large-scaled cracking is prone to form for a sample having high F–T cycles. Moreover, 2D CT images reveal the differential crack network pattern at rock bridge segments and how it is affected by the previous freeze–thaw damage. The crack coalescence and hole collapse patterns and the associated structural deterioration of the rock bridge segment are obviously influenced by the F–T treatment.

Highlights

- Fracture behaviors of pre-flawed hollow-cylinder granite under freeze-thaw-fatigue loads were analyzed.
- Cyclic freeze-thaw weathering influences rock microstructure and geomechanical properties.
- Acoustic emission parameters and spectral analysis reveals the impact of F-T on rock progressive failure.
- The crack coalescence and hole collapse patterns are obviously influenced by the F-T treatment.

1 Introduction

Freeze–thaw weathering is an important factor resulting in deterioration of rock structure and the associated stability of rock engineering in cold regions. Various rock mass instability events emerge in high-altitude and alpine regions (Mateos et al. 2012; Zhou et al. 2016; Kong et al. 2018; Forte et al. 2021), and the irreversible freeze–thaw damage of rock mass after repeated freeze–thaws have attract the attention of many scholars and engineers. Generally, a 9% volume expansion occurs when water freezes to ice, while ice exerts multidirectional tensile stress (i.e., frost heaving force) on rock and would lead to pore expansion and new micro-cracks. When the temperature rises, ice melts into

✉ Yu Wang
  wyzhou@ustb.edu.cn

1   Beijing Key Laboratory of Urban Underground Space Engineering, Department of Civil Engineering, School of Civil & Resource Engineering, University of Science & Technology Beijing, 30 Xueyuan Road, Haidian District, Beijing 100083, People's Republic of China

2   Institute of Geology and Geophysics, Chinese Academy of Sciences, Beijing 100190, China

3   School of Earth Sciences and Engineering, Hohai University, Nanjing 210098, China

water and fills in the pore network of rock, leading to the increase of rock permeability. For engineering rock mass, it is a kind of typical inhomogeneous geometry with plenty of natural discontinuities or flaws, e.g., fissures, joints, cracks and pores that are developed in rock (Cerfontaine and Collin 2018; Li et al. 2021a, b; Miao et al. 2021). The frost heaving force accelerates the propagation of those flaws, and rock geomechanical behaviors are strongly impacted under freeze–thaw conditions. For rock engineering in cold regions, apart from the freeze–thaw fatigue damage acting on rock mass, stress disturbance is also a non-ignorable fatigue load that is applied to the rock mass. The stability of the rock mass is impacted a lot by the blasting vibration, earthquake, drilling, cutting, excavation, etc. (Bagde and Petroš 2005; Xu et al. 2019; Wang et al. 2021a, b, c). As a result, it is crucial to perform related studies on rock containing crack-like and hole-like flaws under coupled freeze–thaw and cyclic loads to ensure the long-term stability of rock constructions.

Previously, plenty of effects have been made to investigate the effect of F–T on rock structural deterioration and the associated fracture behaviors. The influences of F–T temperature, F–T cycle number, rock mineral composition, and porosity on rock geomechanical behaviors have been widely investigated by field testing (Ghobadi and Babazadeh 2015), laboratory testing (Nicholson and Nicholson 2000; Huang et al. 2018), and numerical simulations (Lu et al. 2019; Zhou et al. 2019). The existing research results show that the effect of freeze–thaw on the pre-flawed rock is stronger than that of the intact rock. Nowadays, more and more attention has been paid for the freeze–thaw structural deterioration and the associated mechanical properties of pre-flawed rock. The effect of freeze–thaw actions on the crack coalescence behaviors of rock or rock-like material containing crack-like flaws under static loads has been well understood (Zhou et al. 2019; Wang et al. 2021a; Li et al. 2021a, b).

In recent years, rock mass instability events resulting from the stress disturbance in cold regions emerge frequently, and a number of studies have paid attention to revealing the cyclic or fatigue mechanical behaviors of pre-flawed rock (Zhou et al. 2019; Wang et al. 2021b). In summary, the above studies have greatly broadened the understanding of the failure mechanism of jointed rock subjected to freeze–thaw and cyclic-loading conditions. In actual engineering, the compression failure of sidewalls and shear failure of the shaft well of mining excavation occur frequently, and considerable attention has been paid to the fracture mechanism of rock mass containing cavity-like flaws, i.e., the hollow-cylinder rock mass. The hollow-cylinder rock is very common in rock engineering, such as borehole in petroleum engineering, or the excavation chamber in tunnel or shaft sinking and drifting engineering. Lee et al. (1999) carried out a series of triaxial tests on hollow cylindrical

rock to study the potential influence of the stress path on the rock mechanical behavior. Alsayed (2002) developed a new multi-axial hollow column test apparatus, which demonstrated its multi-axial properties through uniaxial, biaxial, and triaxial compression tests of hollow column sandstone samples. Yang (2018) conducted triaxial compression experiment on hollow-cylinder sandstone samples, and the fracturing evolution was revealed by the X-ray micro CT technique. Wang et al. (2021c) performed multilevel fatigue loading tests on fissure–hole containing rock using acoustic emission monitoring and CT scanning, and the influence of flaw angle on the macro–meso fatigue failure characteristics was revealed. Wang et al. (2022a) conducted fatigue loading tests on granite with different hole orientation, and revealed the macro–meso fracture evolution characteristics of rock that were impacted by the cavity orientation. Although effects have been made to reveal the mechanical properties of hollow-cylinder rock, almost all the investigations are under room temperature. In addition, crack-like flaws usually exist inside rock along with the hole, and few studies have been carried out to investigate the damage and fracture evolution of hollow-cylinder rock containing crack-like flaws.

As a result, in this study, the hollow-cylinder granite with two fissures and a hollow hole were used to investigate the rock fracture evolution characteristics subjected to freeze–thaw and cyclic loads. The macroscopic stress strain description combined mesoscopic acoustic emission and post-test CT scanning is both employed to reveal the influences of the freeze–thaw and cyclic loads on rock macro–meso mechanical behaviors, i.e., strength and deformation feature, stiffness degradation characteristics, AE activities and crack network pattern. The studies are expected to provide a theoretical basis for the predication of the stability of rock engineering in cold regions.

2 Methods

2.1 Granite Material and Sample Preparation

The intact rock blocks were obtained from the Hejing Beizhan iron mine in Xinjiang province, northwest of China. Currently, the Beizhan iron mine is conducting hang-wall ore exploitation, and the design range is between 3536 and 3380 m at the east of the open pit. The designed mining method is sublevel open stop mining, and several shaft wells have been excavated to recycle the ore. Referring to the recommended method by the American Society for Testing and Materials (ASTM 2007), all the tested rock samples were prepared as cylindrical shape with a diameter of 50 mm and height of 100 mm. The tested rock samples were polished to ensure that the parallelism and the non-uniformity error is less than 0.1 mm and 0.05 mm, respectively. To mimic the
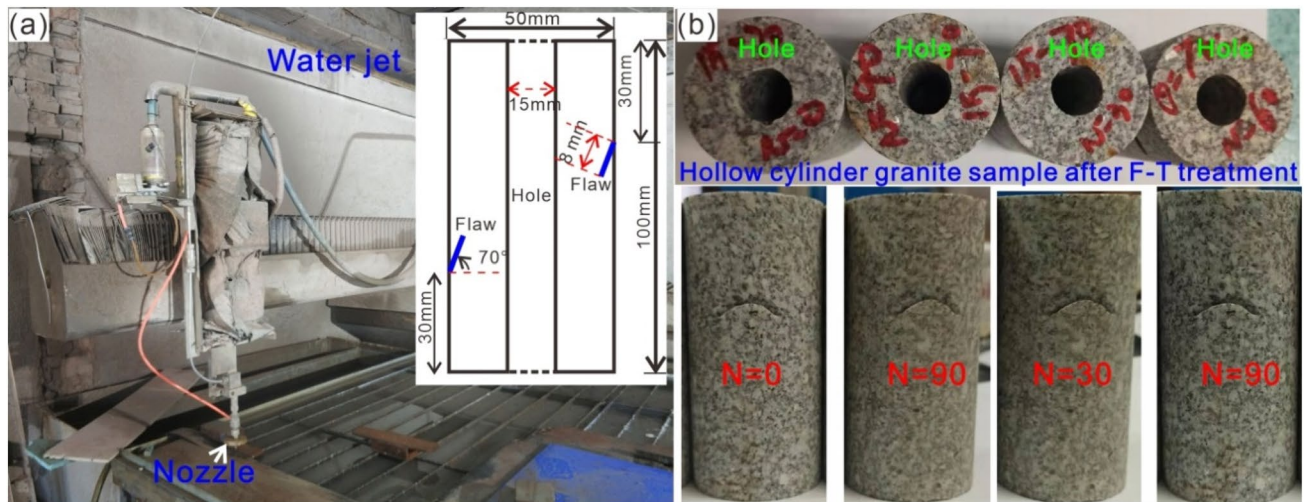
Fig. 1 Perpetration of the hollow-cylinder granite samples containing two fissures. (**a** Water jet was used to produce hollow hole and two opposite flaws. **b** Typical rock samples after freeze–thaw treatment.)
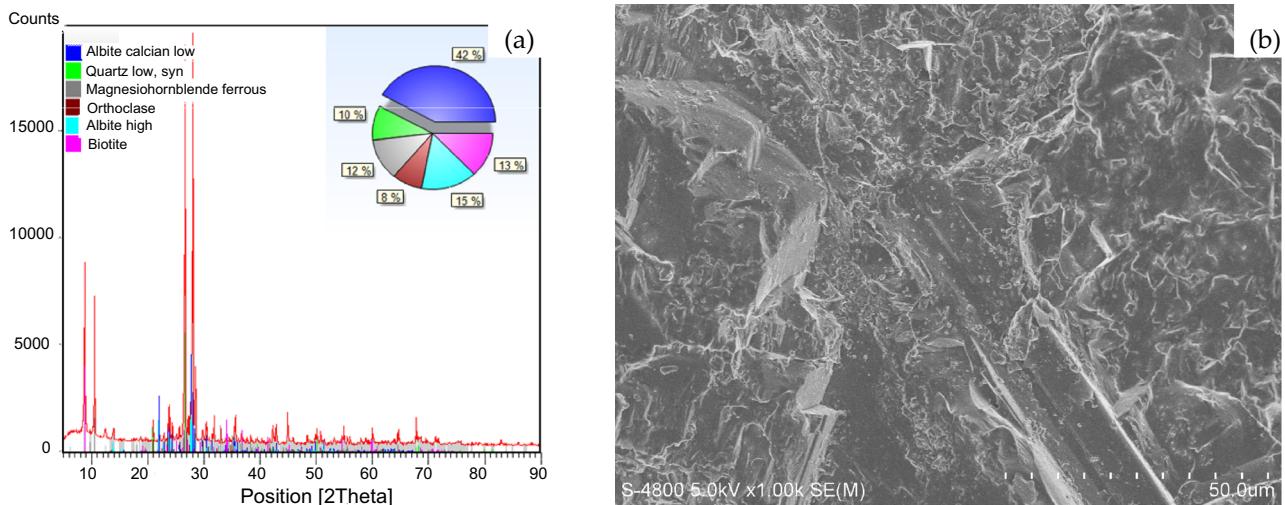

Fig. 2 Representation of the mesoscopic structure of the granite material; **a** and **b** the results of XRD and SEM, a magnification of 1000 times is used here

shaft well in the hang-wall ore exploitation, the rock samples were prepared with holes and flaws in them. Preparation of the two flaws and central hole is carried out using low disturbance water jet; see Fig. 1a. Before preparation of the tested rock, we select rock samples having roughly the same mesoscopic structure by ultrasonic measurement, i.e., the homogeneity of them is almost the same. The diameter of the hole is set to be 15 mm based on Saint-Venant's principle that is less than 1/3 of the rock diameter, to minimize the stress effects from the boundary of the core. The length of the flaw is set to be 8 mm. Two fissures with an angle of 70° were cut at opposite sides of the hollow-cylinder granite; see

Fig. 1b. A total of ten samples were prepared to conduct the freeze–thaw fatigue loading tests.

XRD result in Fig. 2a indicates the mineral composition of the tested granite. It is found that the rock is mainly composed of magnesium amphibole (12%), albite (75%), orthoclase (8%), quartz (10%) and biotite (13%), respectively. SEM result in Fig. 2b reveals the mesoscopic structure of the rock, the tested rock has inhomgeneous structure and several micro-cracks and mineral interfaces were observed. In addition, a large number of pores of different sizes are distributed among the minerals.
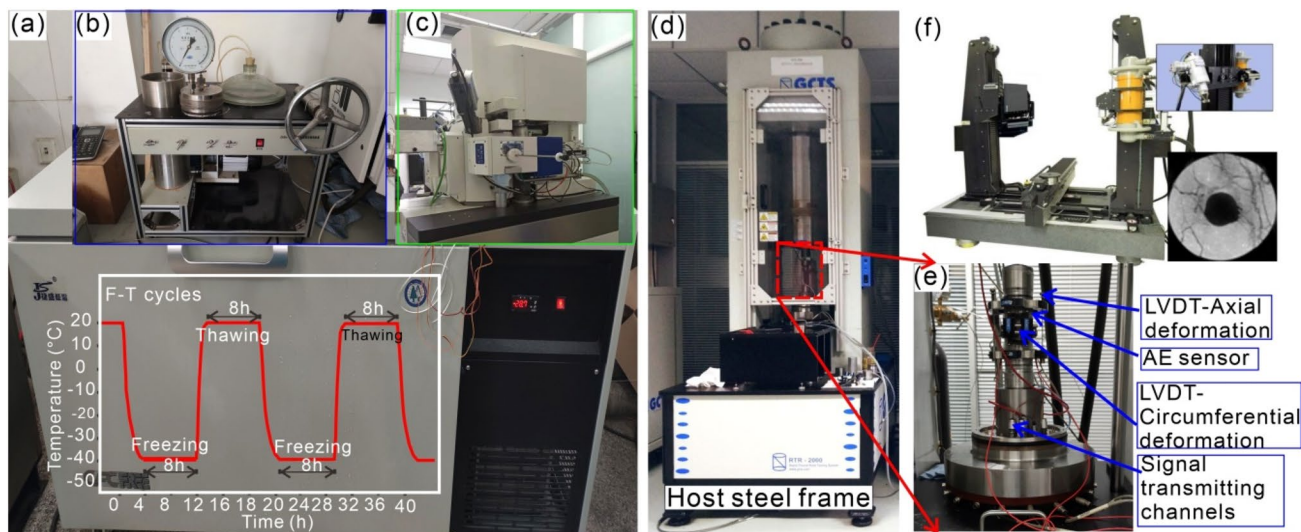
Fig. 3 The testing apparatus used in this work. (**a** The ultralow temperature environmental chamber; **b** vacuum saturation device; **c** scanning electron microscope; **d** GCTS 2000 rock mechanics test-ing machine; **e** THE axial and circumferential LVDTs; **f** The 420 kV industrial CT machine.)

2.2 Testing Equipment

The testing devices include vacuum saturation device (Fig. 3a), ultralow temperature environmental box (Fig. 3b), scanning electron microscope (Fig. 3c), GCTS RTR 2000 rock mechanics machine (Fig. 3b) and industrial CT machine (Fig. 3e). The tested samples were first subjected to saturation treatment in a vacuum saturation device in advance, and different number of F–T cycles in an ultralow temperature environmental box were applied to the saturated rock samples. Afterward, the fatigue loading tests were carried out on the pre-flawed hollow-cylinder granite using a GCTS RTR 2000 system. The system features closed-loop digital servo control and are managed using advanced software and electronics, allowing for complete rock test automatically. The two axial LVDTs devices were installed at the vertical direction to measure axial deformation, and a circumferential LVDT device was installed at the middle of the rock sample to obtain radial strain (Fig. 4b). The maximum dynamic loading frequency of the machine is 10 Hz. The stiffness of the host steel frame is 10 MN/mm, and the maximum loading stress of 4600 kN can be applied to rock samples. During cyclic-loading experiment, rock axial strain, radial strain, and axial stress can be collected at the same sampling frequency.

During the mechanical tests, an acoustic emission technique was employed to record the fracturing information, including the AE ring count, energy count, amplitude, peak frequency, etc. After the mechanical experiments, typical samples were performed: X-ray CT scanning to obtain the crack coalescence pattern between the two flaws. In this work, an industrial CT machine with its voltage of 420 kV and power current of 8 mA was used for imaging, as shown in Fig. 3f. The scanned voxel size was 0.083 mm × 0.083 mm × 0.083 mm. Based on the CT images, the influence of freeze–thaw on the crack coalescence and hole spalling and collapse can be clearly visualized.

2.3 Testing Procedures

All the tested pre-flawed granite samples were subjected to saturation treatment and then placed in an ultralow temperature freeze–thaw environmental box. Afterward, multistage cyclic-loading test was performed on the freeze-thawed samples. The detailed testing procedure is summarized below:

(1) Rock saturation treatment. The samples were placed in a vacuum saturation device for 24 h before the freeze–thaw treatment.

(2) Rock freeze–thaw treatment. The upper and lower temperatures for FT testing were chosen according to the actual temperature variations at the Beizhan open pit over the course of a year. The temperature at the Beizhan iron mine can reach − 40 °C during the night in winter, and a permafrost state lasts during the whole winter. In summer, the temperature is around 20 °C during the daytime, so that frozen water in the pores of the rock will melt triggering a thawing process. As a result, an 8-h freezing period (− 40 °C) and an 8-h thawing period (+ 20° C) were applied to the rock to simulate FT cycles of the rock in the mine. In addi-
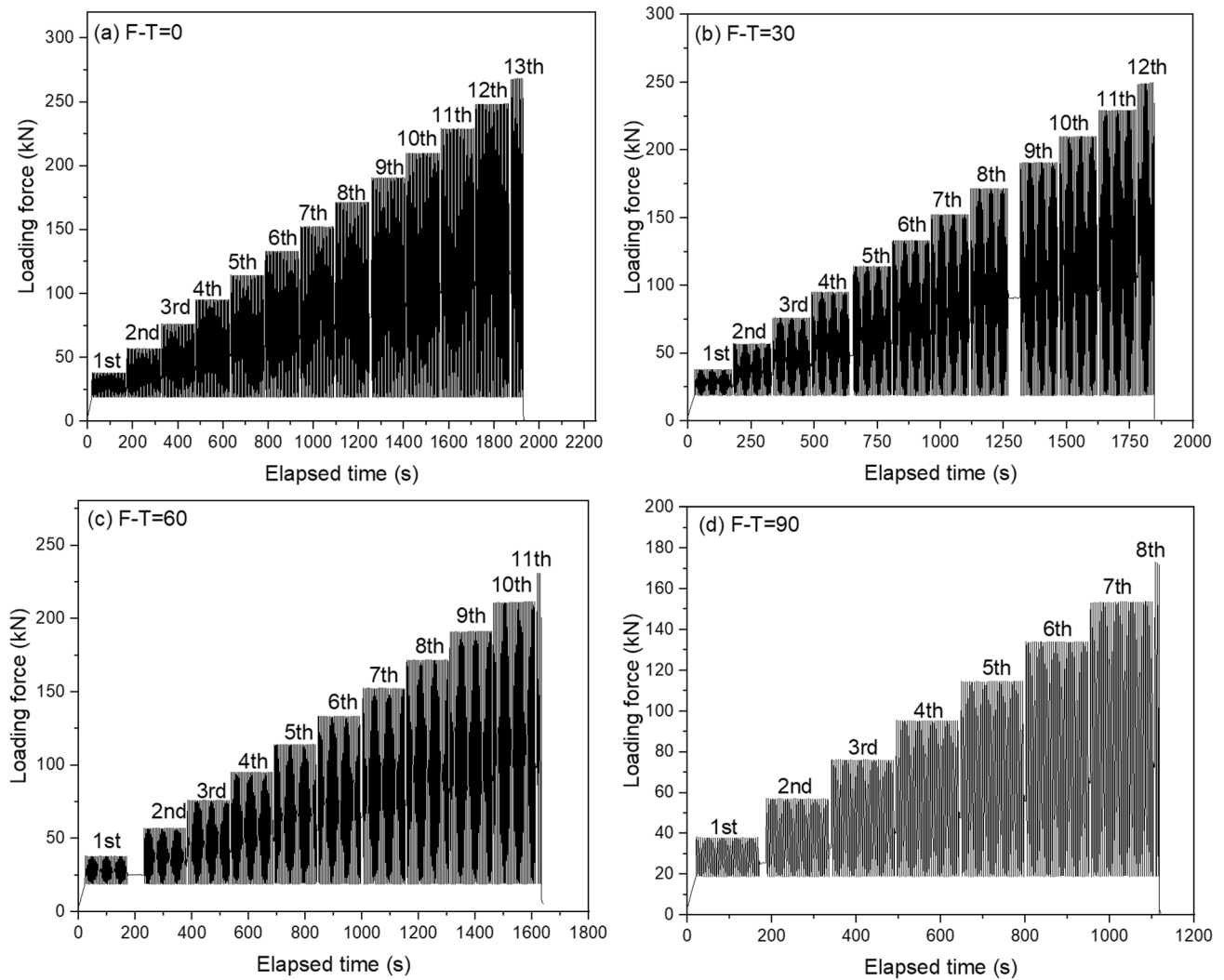
Fig. 4 The loading paths of the tested hollow granite containing two flaws. (**a–d** Rock samples experiencing 0, 30, 60, and 90 F–T cycles, respectively)

tion, 8 h is long enough to reach a completely frozen state or thawed state. In the laboratory, the saturated sample was frozen in the F–T machine at − 40 °C for 8 h, then the sample was taken out of the refrigerator and thawed in water at 20 °C for 8 h; this is a complete F–T cycle. It ensures that the influence of FT on rock mechanical properties is obvious. We measured the ultrasonic velocity of rock samples after one or two FT treatments, and rock samples having obvious velocity difference were used to conduct the cyclic-loading tests. The FT cycle for the tested rock is determined to be 0, 30, 60, and 90, respectively.

(3) Multistage cyclic-loading test. The sample was first subjected to a static loading to a stress of 10 MPa at a constant displacement rate of 0.06 mm/min (i.e., $1.0 \times 10 − 5 \text{ s}^{-1}$). Following the static loading path, the pre-flawed hollow-cylinder granites were applied

to cyclic loading with a dynamic frequency of 0.2 Hz. That is, a cycle with a loading and unloading duration can be completed within 5 s. In the fatigue loading process, in the first cyclic dynamic loading stage, sinusoidal cyclic loads controlled by stress is applied, and the stress amplitude is 10 MPa. In each subsequent cyclic-loading stage, the stress amplitude increased by 10 MPa and was controlled by the type of sinusoidal cyclic loads. The stress cycle continues in this manner until the sample finally fails. In each dynamic cyclic-loading stage, a total of 30 stress cycles are applied to granite samples. Therefore, multistage or multilevel cyclic-loading paths were applied to the fissure-contained hollow-cylinder granite samples. Figure 4 displays the detailed cyclic-loading paths for the samples experiencing 0, 30, 60, and 90 F–T cycles, respectively.

(4) During the cyclic-loading process, acoustic emission monitoring was conducted to detect crack initiation, propagation, and coalescence behaviors. A series of acoustic emission analysis methods were used to reveal the influence of the previous freeze–thaw damage on the deterioration of granite samples containing two kinds of defects. These methods include: calculating the acoustic emission event rate (or cumulative number), calculating the acoustic emission energy, checking the amplitude distribution, and studying the frequency characteristics of the signal.

(5) After the cyclic-loading experiment, CT scanning was employed to obtain the mesoscopic failure pattern at the rock bridge segment.

3 Results and Analyses

3.1 Effect of F–T on Rock Mesoscopic Structure Changes

The previous freeze–thaw damage is analyzed from SEM pictures of the rock matrix, as shown in Fig. 5. The rock slice is obtained from the inwall of the hollow hole and observed using a field emission scanning electron microscope (FIB-SEM). Figure 5 presents the SEM pictures with different magnification times. For rock without F–T treatment, it is shown that the rock is with high compactness, and no pores or micro-cracks were observed. For rock with 30 F–T treatment, some micro-cracks were distributed sporadically and the compactness became weak. For rock with 60 and 90 F–T cycles, the pores and micro-cracks increase, which is caused by the freeze–thaw treatment. The frost-heaving force as a tensile stress accelerated the development of flaws. The flaw scale is the largest for a rock subjected to the maximum F–T cycles of 90.
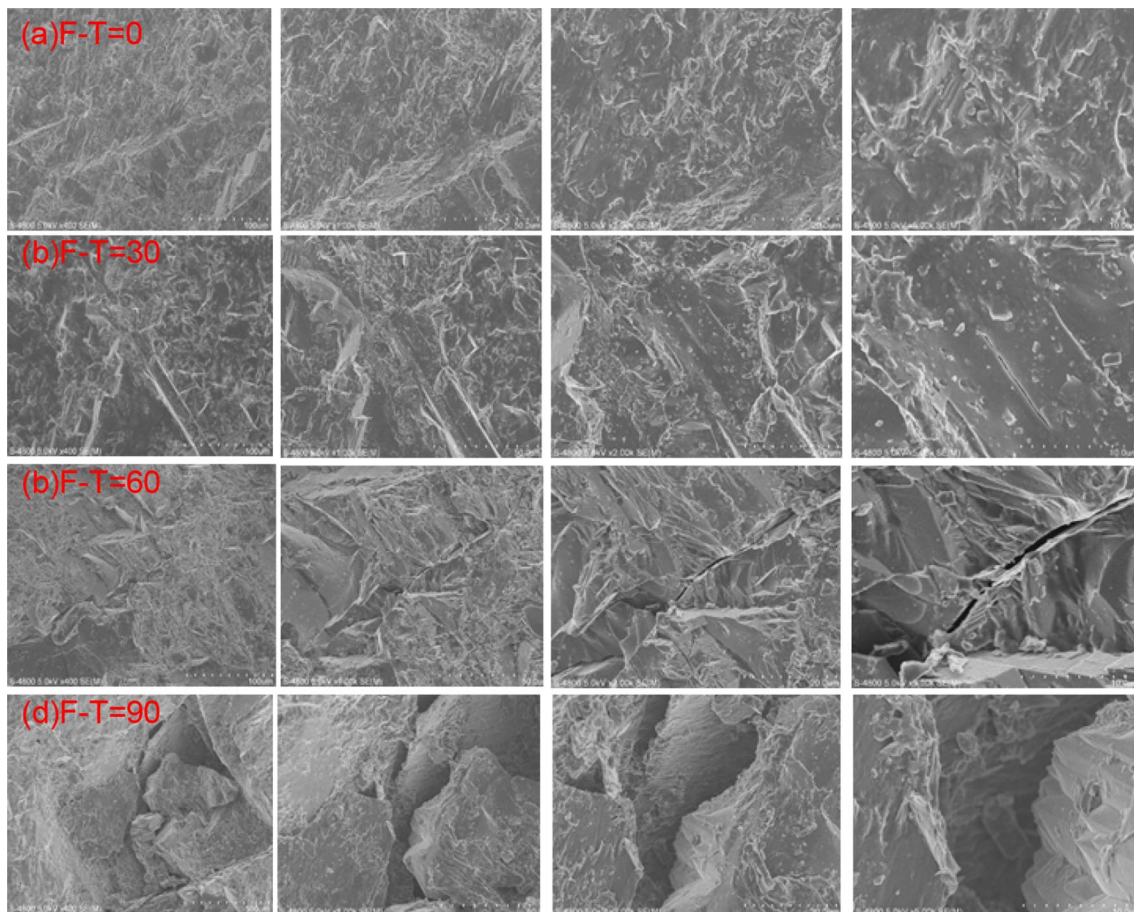

Fig. 5 SEM pictures of the mesoscopic structure change of rock subjected to different F–T cycles
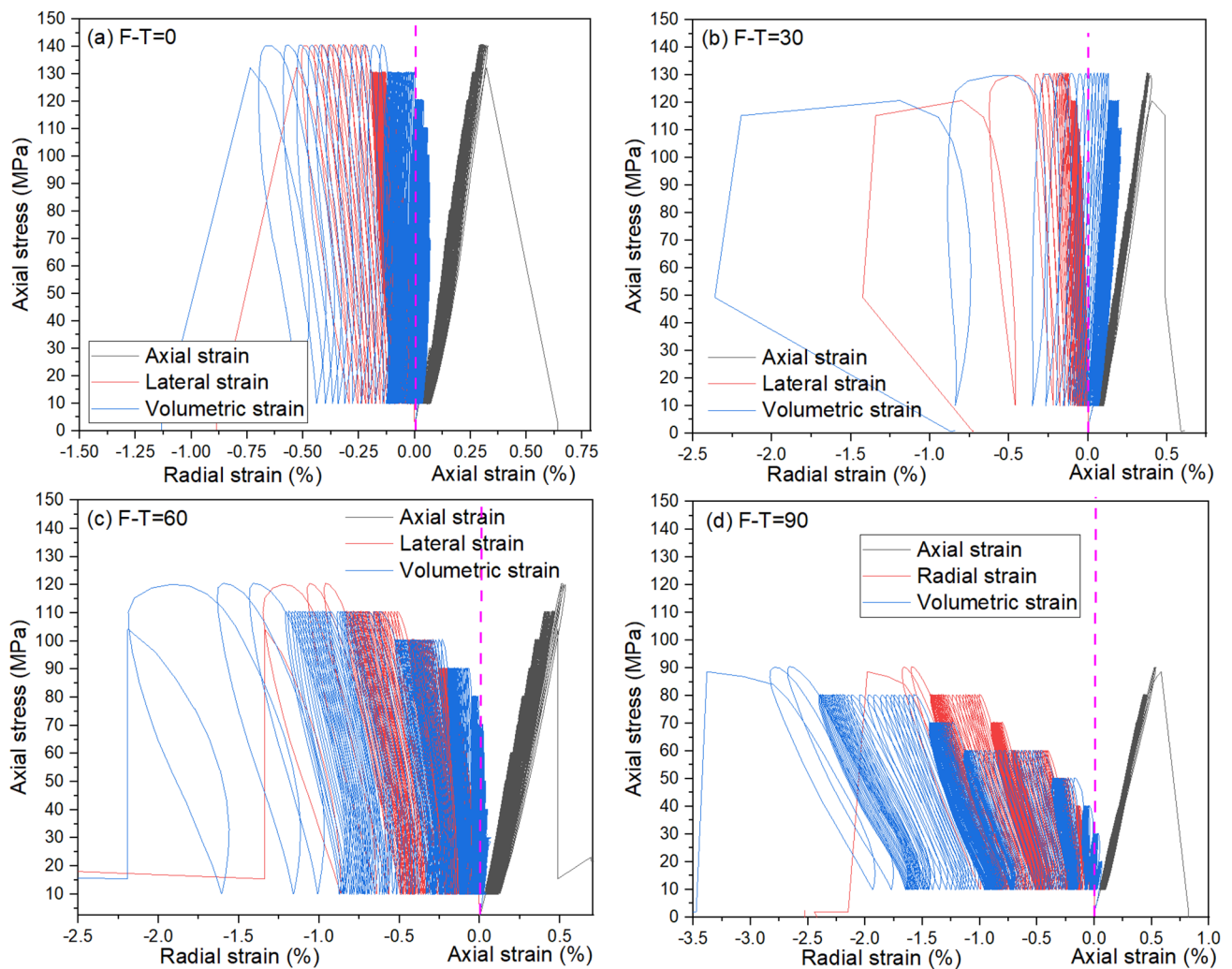
Fig. 6 The axial, radial, and volumetric stress–strain responses of typical hollow granite containing two flaws. (**a–d** Rock samples subjected to 0, 30, 60, and 90, freeze–thaw cycles.)

## 3.2 Representative Stress–Strain Curves

The axial, radial, and volumetric stress–strain curves for the pre-flawed hollow-cylinder granite are plotted in Fig. 6. It must be noted that the radial strain in this work is obtained by the radial LVDT, and should be corrected as the suggestion method by Masoumi et al. (2015). However, because all the experiments were performed under the same loading conditions and using the same measurement device, herein, the radial strain was not corrected. Owing to the differential freeze–thaw damage on the rock samples, their capacity to resist external loads is different; as a result, rock fatigue strength, deformation, and lifetime differ with F–T cycles. The cyclic-loading stage is 13, 12, 11, and 8, and the corresponding loading cycle is 372, 344, 304, and 212, respectively. In addition, crack coalescence and hole spalling patterns display different responses that can be reflected on the stress–strain curves.

Although all the freeze-thawed rocks experienced freeze–thaw cycles, the maximum axial strain is less than 0.5%, displaying strong brittleness characteristics. The peak strain is 0.316%, 0.403%, 0.492%, and 0.575%, respectively.

The volumetric strain curves marked in blue color are the combined reflection of rock deformation. The loading curve and unloading curve are observed to clearly not overlap, and a hysteresis loop forms at each loading and unloading moment. The formation of the hysteresis loop indicates the occurrence of plastic deformation inside the rock, and the irreversible deformation varies during the whole loading process. At the initial stage, which is several cyclic-loading stages before rock failure, the hysteresis loop is sparse and then gets very dense and develops steadily with increasing cycle. The sparse pattern at the beginning of a loading stage implies the generation of relatively large damage and the

Table 1 Summarization of the mechanical parameters of the tested granite samples

Sample ID	L×d (mm×mm)	F–T cycle	Peak axial strain (%)	Peak lateral strain (%)	Peak volumetric strain (%)	Loading stage	Loading cycles
FU-0-1	100.01×49.39	0	0.316	− 0.528	− 0.74	13	372
FU-0-2	99.89×50.05	0	0.323	− 0.644	− 0.965	13	387
FU-30-1	99.62×49.95	30	0.403	− 1.339	− 2.275	12	344
FU-30-2	99.62×49.95	30	0.415	− 1.326	− 2.237	12	354
FU-60-1	99.89×50.05	60	0.492	− 1.342	− 2.192	11	304
FU-60-2	99.62×49.95	60	0.445	− 1.506	− 2.567	11	315
FU-90-1	99.89×50.05	90	0.575	− 1.982	− 3.389	8	212
FU-90-2	99.62×49.95	90	0.616	− 2.211	− 3.806	8	234
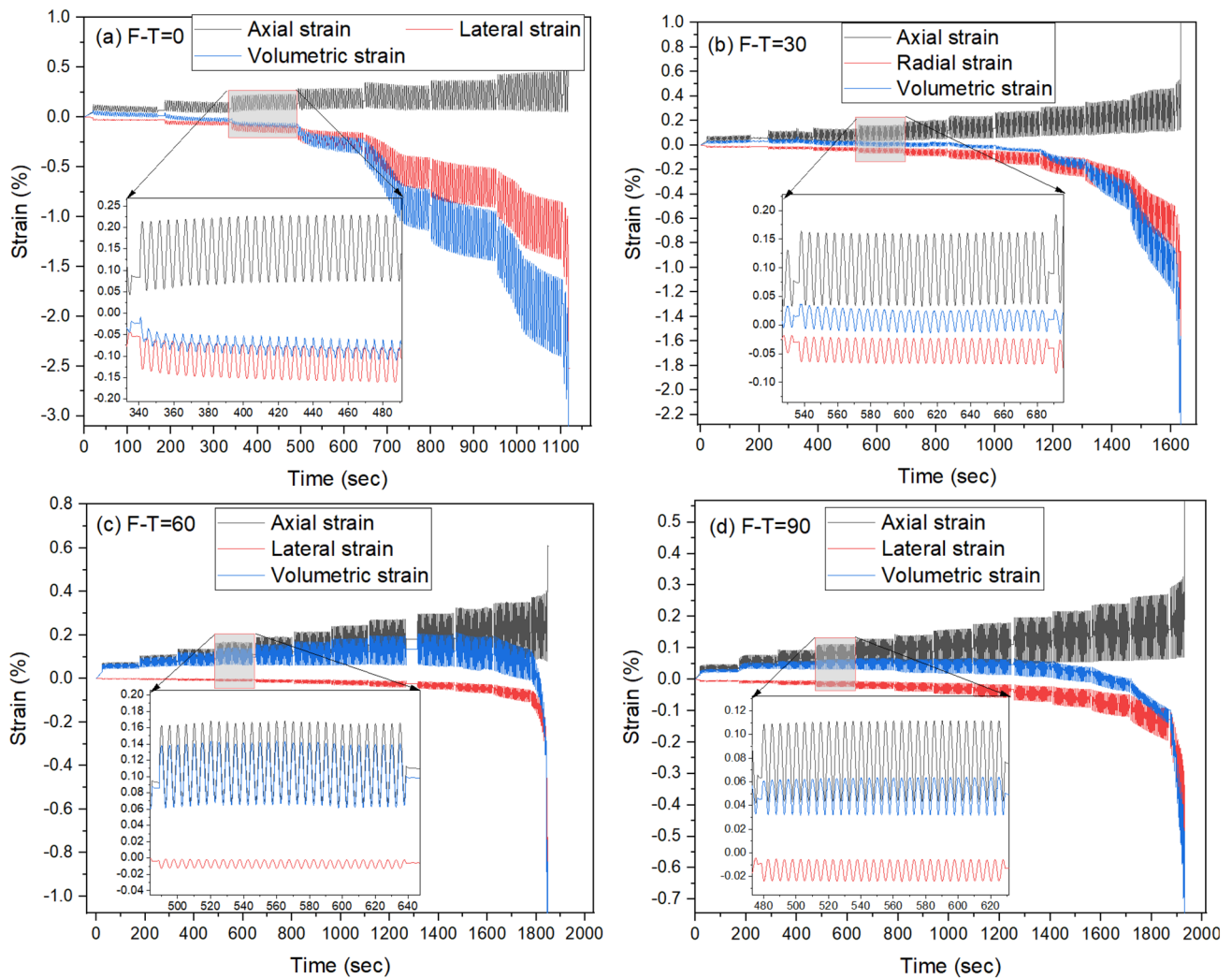
Fig. 7 Deformation evolution of the hollow-cylinder granite samples under multistage cyclic loads (**a–d** Plots of maximum axial strain, radial strain and volumetric strain for samples subjected to 0, 30, 60, and 90, freeze–thaw cycles)

damage increases with increasing cyclic stage. However, at the last cyclic stage, it is observed that the hysteresis loop becomes increasingly sparse until rock failure. Affected by

the freeze–thaw damage, the failure pattern may be different, which can also be reflected from the pattern of the hysteresis loop at the last cyclic-loading stage. For the hollow-cylinder

granite subjected to 0 and 30 F–T cycles, the number of hysteresis loop is more than that of rock subjected to 60 and 90 F–T cycles. The difference in the hysteresis loop shape reflects the different fracture mechanism, and the area of the hysteresis loop reflects the energy dissipation during rock deformation. The rock strength and deformation parameters are listed in Table 1.

3.3 Deformation Behaviors of Pre-flaw Hollow Granite

During the entire loading process, the evolution of axial, radial, and volumetric strain against experimental time is shown in Fig. 7. A similar trend is observed in that the deformation growth rate became faster and faster with increasing loading time. The sudden increase of deformation rate indicates the occurrence of unstable crack propagation inside the rock. According to the studies of the monotonous loading stress–strain curves, the onset point of the sudden increase corresponds to the crack coalescence point. The cyclic-loading curves are also controlled by the monotonous loading curve. It is observed that the developed trend of the volumetric strain is similar to the radial strain. The growth rate of radial strain is larger than the volumetric strain at the first several cyclic-loading stages; however, the volumetric growth rate of volumetric becomes faster than the radial strain after several loading stages, and the rapid growth of the volumetric strain results in the final failure rock. At the rock failure moment, it is shown that the volumetric strain is larger than the radial strain.

To clearly observe the deformation evolution characteristics, Fig. 8 presents the relationship between the axial strain, radial strain, and cycle number in each stage. It is observed in Fig. 8a–d that the change of axial strain within a cyclic stage is relatively small before the finial loading stage; however, the increasing rate of axial strain between each cyclic stage increases quickly. The accumulative damage at the previous cyclic-loading stage has an obvious impact on rock axial deformation. At the start of each cyclic-loading stage, the axial deformation grows relatively fast and then becomes steady within a cyclic stage; however, at the final loading stage, axial deformation grows quickly until rock failure. Figure 8e–h presents the change of radial strain caused by the crack propagation and hole spalling during rock deformation. It should be noticed that it only reflects the radial expansion deformation at the position of circumferential LVDT chain. The interactions between the fissures and hole are strongly impacted by the previous freeze–thaw damage, the growth rate of radial deformation becomes faster and faster, and the sudden collapse of the pre-hole causes a sharp increase of radial deformation. The upper lateral strain is larger for a rock sample subjected to 0 and 30 F–T cycles than that of 60 and 90 F–T cycles.

The volumetric strain ε_v in Fig. 9 is calculated as $\varepsilon_1 + 2\varepsilon_3$ and reflects the comprehensive deformation of the axial deformation and radial deformation. The evolution trend of volumetric strain is similar to that of the radial strain. The loaded rock samples display different evolution characteristics for the volumetric strain, and the inflection moment for rock from volume compression to expansion is different. The volume inflection occurs at the 12th, 11th, 5th, and 2nd cyclic stages for rock sample subjected to 0, 30, 60, and 90 F–T cycles. In this work, for the tested hollow-cylinder granite with flaws, the volume change is impacted by the interaction between the pre-flaws and hole. The two fissures propagate and finally communicate with the vertical hollow hole, and this causes the deformation and collapse of the hole.

3.4 Rock Stiffness Degradation During Cyclic Loads

Based on the cyclic stress–strain curves in Fig. 6, two elastic parameters of secant modulus and Poisson's ratio were analyzed to reveal the stiffness degradation of the tested granite, as plotted in Figs. 10, 11. The secant modulus here is defined as the gradient of the upper stress to lower stress of each cycle at the loading stage, and the Poisson's ratio is defined as the upper lateral strain to the upper axial strain of each cycle at the loading stage. The secant modulus in Fig. 10 shows that it presents a decreasing trend as cycle number grows within a loading stage, and the decreasing rate becomes faster especially at the last few cyclic-loading stage. The decrement of secant modulus reflects the stiffness degradation of rock exposed to repeated loading and unloading. Influenced by the previous freeze–thaw damage (i.e., F–T treatment), the secant modulus is maximum for a sample without the F–T cycle, and it is minimum for a sample with 70 F–T cycles. The differential structure degradation is mainly caused by the previous freeze–thaw damage. Under cyclic-loading stage, the decrement of the secant modulus is caused by the crack propagation and hole collapse.

Another parameter used to represent the non-linear fracture evolution and stiffness degradation is the Poisson's ratio, as shown in Fig. 11. It increases quickly in the initial cycles within a cyclic stage and then becomes steady. At high cyclic-loading stage, the Poisson's ratio grows fast until the maximum value of 0.5. The Poisson's ratio can reflect the incremental degree of radial deformation, and it is observed that the radial expansion becomes severe at cyclic stages near rock failure. The results in Fig. 9 also indicate that the previous freeze–thaw damage influences the damage accumulation and plastic deformation exposed to cyclic loads, and a different loading stage occurs for the rock to get the maximum value of Poisson's ratio. The cyclic stage is 11, 10, 4, and 2, respectively, for rock sample subjected to F–T cycle of 0, 30, 60, and 90, respectively. The increasing rate
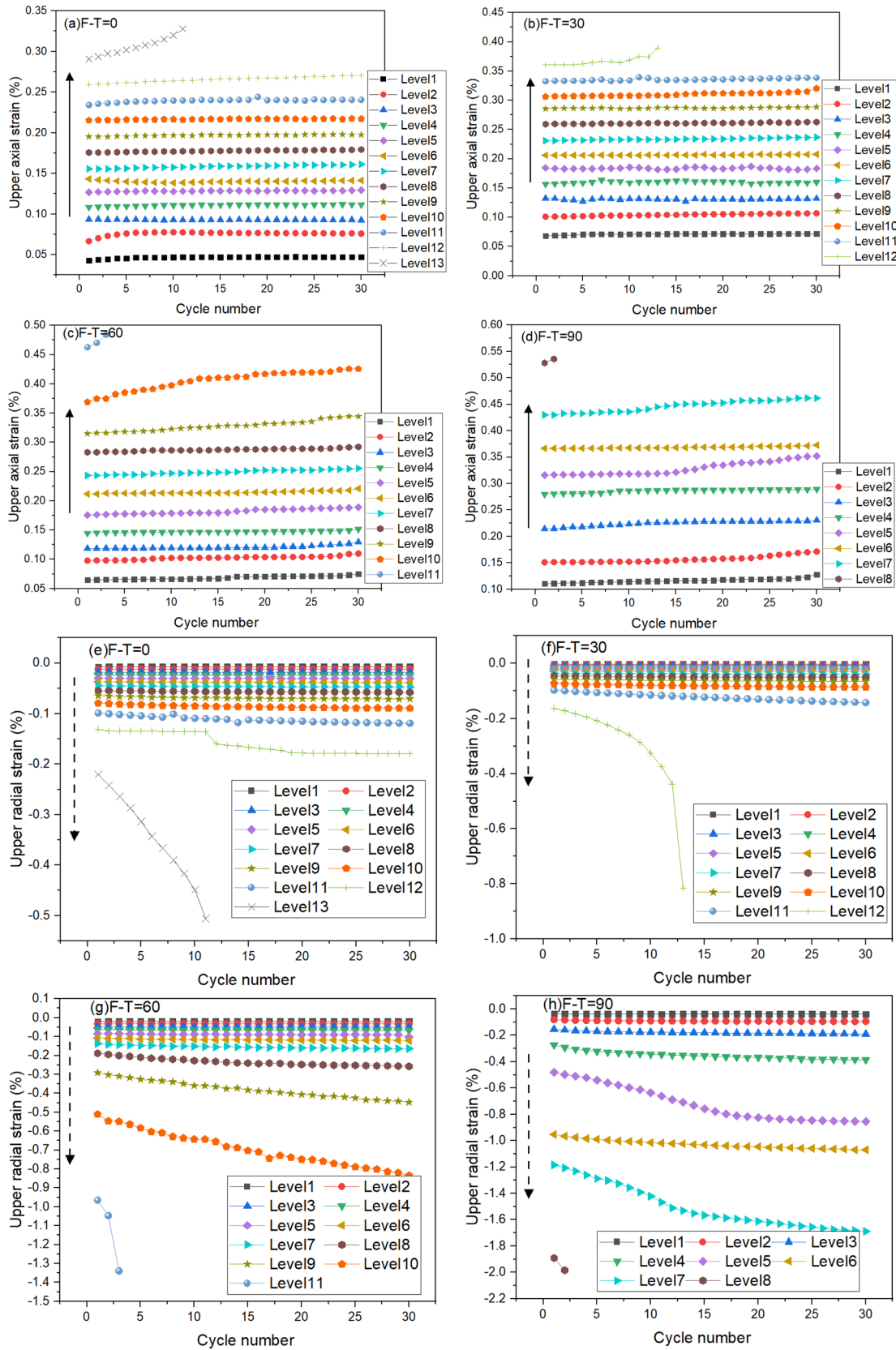
Fig. 8 The maximum deformation charactersitics of the tested granite samples experiencing F–T cycle of 0, 30, 60, and 90, respectively, at different loading level (stage). (**a–d** Plots of the maximum axial strain against cycle number; **e–h** plots of the maximum radial strain against cyclic number.)
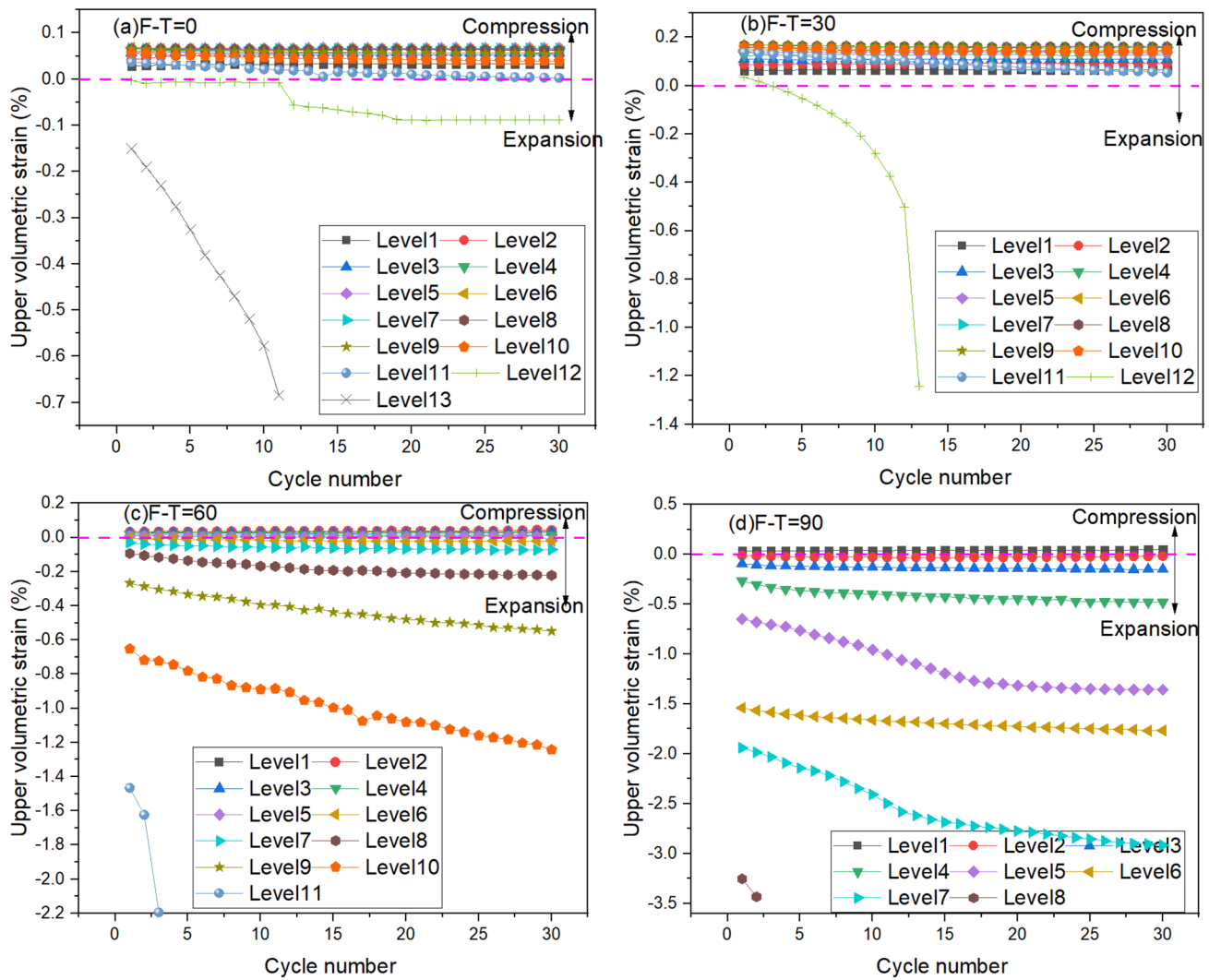
Fig. 9 The maximum volumtric strain of the tested granite samples during cyclic-loading tests (**a–d** The F–T cycle is 0, 30, 60, and 90, respectively.)

of the Poisson's ratio increases with increasing F–T cycles, indicating the influence of freeze–thaw damage on structural deterioration.

3.5 Characterization of AE Count/Energy

It is helpful to grasp the mesoscopic fracture mechanism, including crack initiation, propagation, coalescence, and hole collapse of rock, by counting AE hits and AE energy (Muñoz-Ibáñez et al. 2021). The recorded AE activity pattern reflects the fracturing characteristics of rock. Figure 12a–d shows the changes of AE ring counts, accumulative AE ring count, axial stress and experimental time. It is found that many AE signals are generated at the beginning of each cyclic-loading stage, and then AE activities become weak within a cyclic-loading stage. The increases of stress amplitude further lead to the increase of AE ring counts;

afterward, AE activities display a silent pattern within a cyclic-loading stage. This result implies that the damage at the stress-increasing stage is larger than at the cyclic-loading stage. The patterns of the output AE activities are obviously different owing to the differential freeze–thaw damage, i.e., the different F–T cycles. For rock with low F–T cycle number of 0 and 30, the occurrence and skip of AE events at each cyclic-loading stage are not obvious, several AE activities were recorded reflecting steady crack propagation mode, and the AE events surge at the final cyclic-loading stages. Relatively few AE events were recorded before the last cyclic-loading stage for these two samples, and the large fracturing events are concentrated at the rock failure stage. However, for rock subjected to 60 and 90 F–T cycles, AE activity is obvious at each cyclic-loading stage, and the AE ring counts at the failure stage are less than rock samples subjected to low F–T treatment.
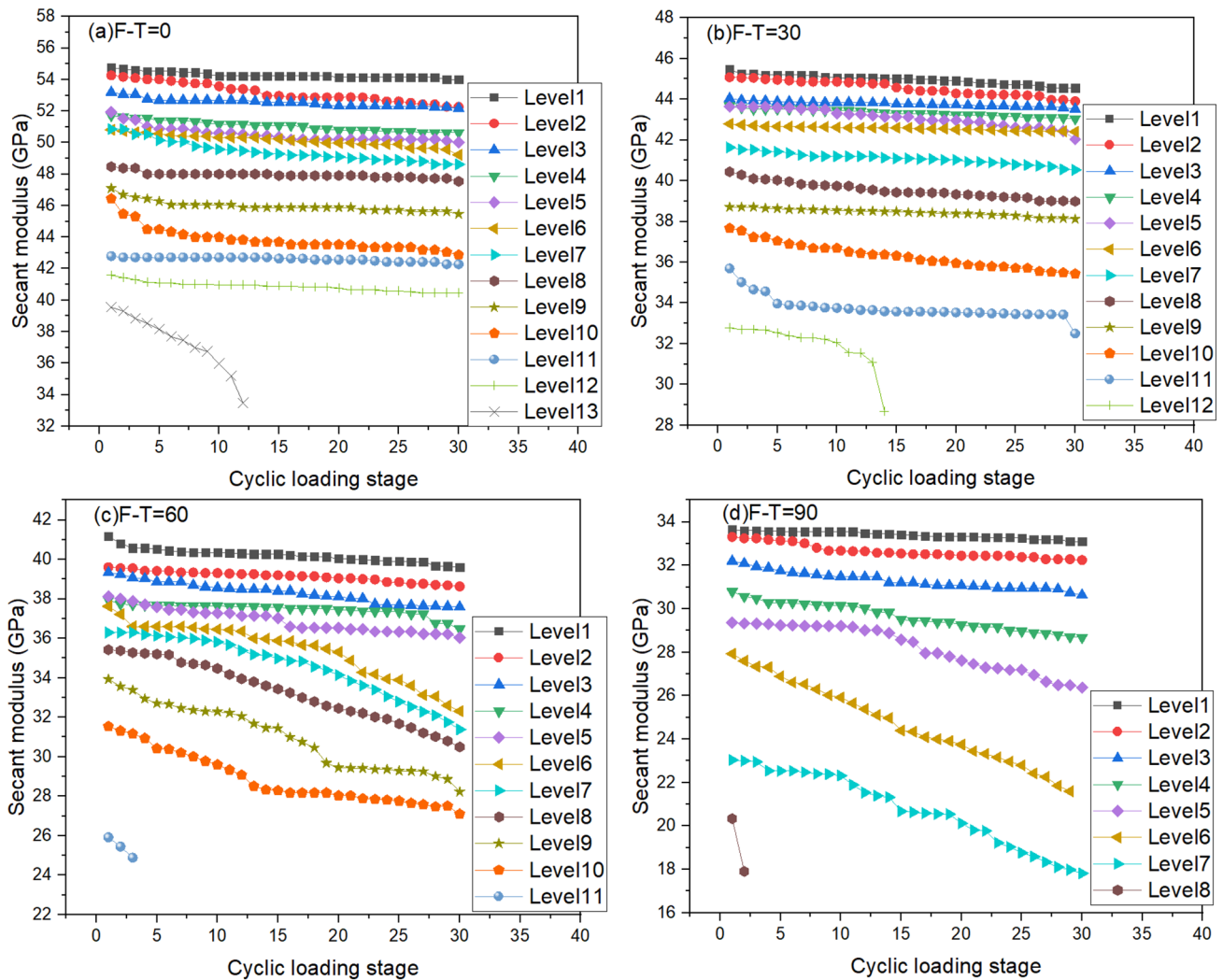
Fig. 10 Depiction of secant modulus with cycle number for the pre-flawed hollow-cylinder granite at various cyclic-loading stages (**a–d** The rock samples subjected to 0, 30, 60, and 90, freeze–thaw cycles.)

Apart from counting the AE events to reveal rock fracture evolution, the released strain energy during rock failure is also recorded by the AE sensors. The evolution curves of AE energy, AE accumulated energy and experimental time are plotted in Fig. 12e–h. The released energy displays different patterns at the stress-increasing stage and cyclic-loading stage. Smaller released energy was received by the AE sensors for rock failure at the cyclic-loading stage. A sudden energy skip is observed at the stress-increasing moment, and high AE energy release is recorded under the sudden formation of macroscopic cracks, especially at the last several cyclic-loading stages. Similar to the AE ring count curves, the released energy curves also present a different pattern for rock experiencing a different F–T cycle.

As for the cumulative AE ring count and energy curves in Fig. 13, it is found that all the cumulative curves show a stepwise growth pattern, but the growth trend is different.

The shape of the accumulative curve is affected by the rock bridge length in the pre-flawed granite samples. The growth rate of the accumulative AE event/energy increases with increasing F–T cycle. However, the total AE event number decreases with increasing F–T cycle. It can be observed that the sudden skip points and periods of relative calm occur alternately, indicating that the cracks propagate further only when the elastic strain energy accumulates to a certain extent. The skip position corresponds to the stress-increasing point, which reflects the greater AE energy release at this time. The concentration of AE events also reflects the energy release during rock fracturing, and the intensity of energy release is the largest and smallest for rock experiencing 0 and 90 F–T cycles, respectively.
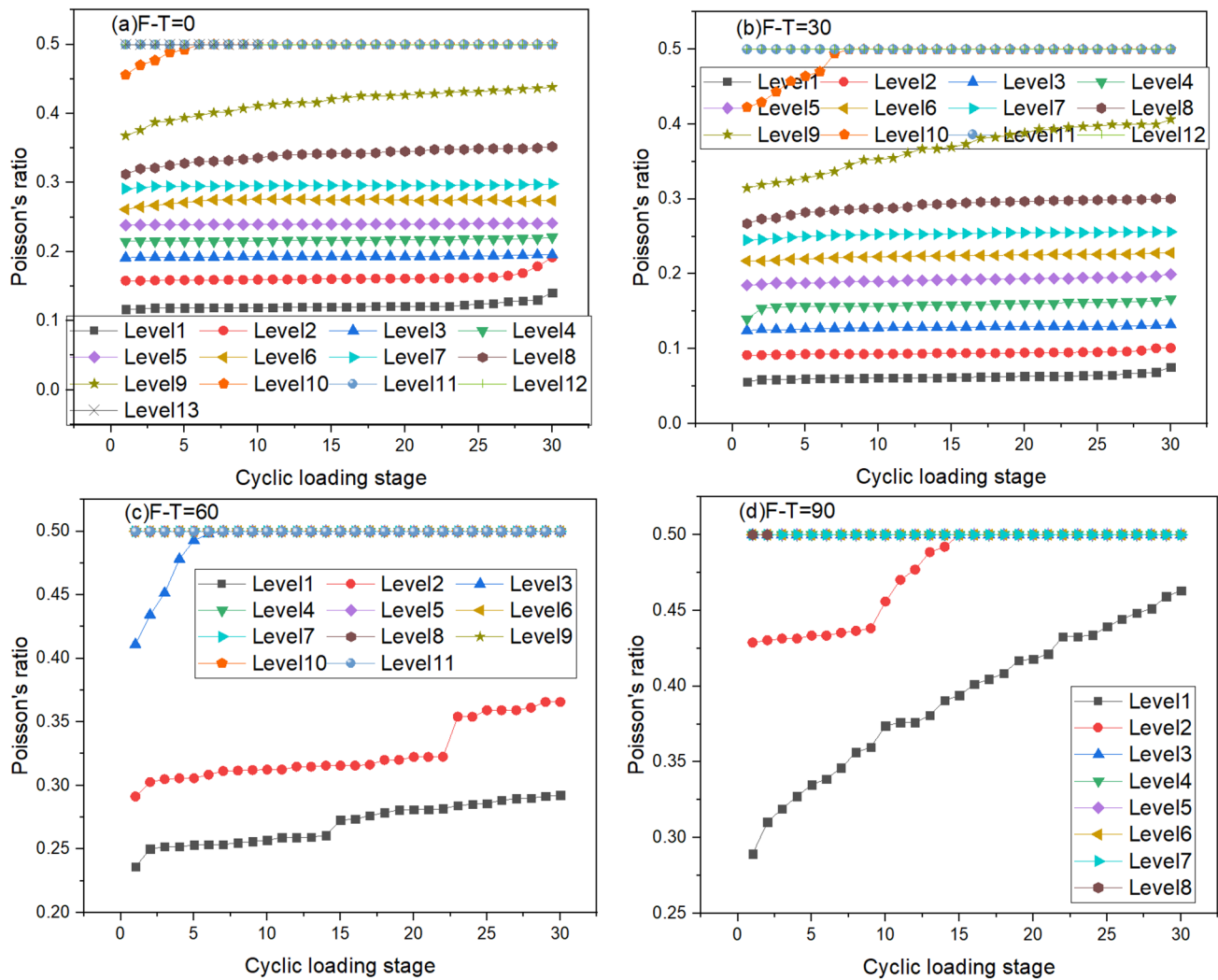
Fig. 11 Depiction of Poisson's ratio with cycle number for the pre-flawed hollow-cylinder granite samples subjected to 0, 30, 60, and 90, freeze–thaw cycles

3.6 AE Amplitude Characteristics During Rock Deformation

As an important parameter to represent rock fracturing, the AE amplitude reflects the damage level and instability of rock material. A correlation between the fracture energy and AE amplitude has been found (Scholz 1968; Mogi 1981; Yang et al. 2020). Investigations on the changes of AE amplitude distribution are good to understand crack propagation behaviors. The distribution of the AE amplitude during multistage cyclic loads is shown in Fig. 14. From the scatter distribution, it reveals the fact that the number of AE signals is larger for rock experiencing relatively small F–T cycles (i.e., 0 and 30 F–T cycle) than those with high F–T cycles (i.e., 60 and 90 F–T cycle). Under low loading level, the AE amplitude is relatively high for rock subjected to less F–T cycles, indicating the occurrence of strong brittle fracture.

The crack initiation, propagation and communication of the hole and fissure are relatively easy for rock subjected to high F–T cycles, implying that their peak strength is relatively low. AE signal with high amplitude occurs at the stress-increasing stage, and an obvious skip can be observed from the scatter distribution, indicating that the released energy is larger for rock at the stress-increasing moment. This result indicates that large damage occurs at the stress-increasing stage, and this is consistent with the above results. At the final failure stage, plenty of high-amplitude AE signals are generated, and the elastic energy stored inside the rock is released abruptly.

Frequency description is analyzed to study the distribution law of AE amplitude during the cyclic-loading process; see Fig. 15. It is shown that the number of high-amplitude events decreases with the increase of F–T cycle; in addition, the total AE count that corresponds to high
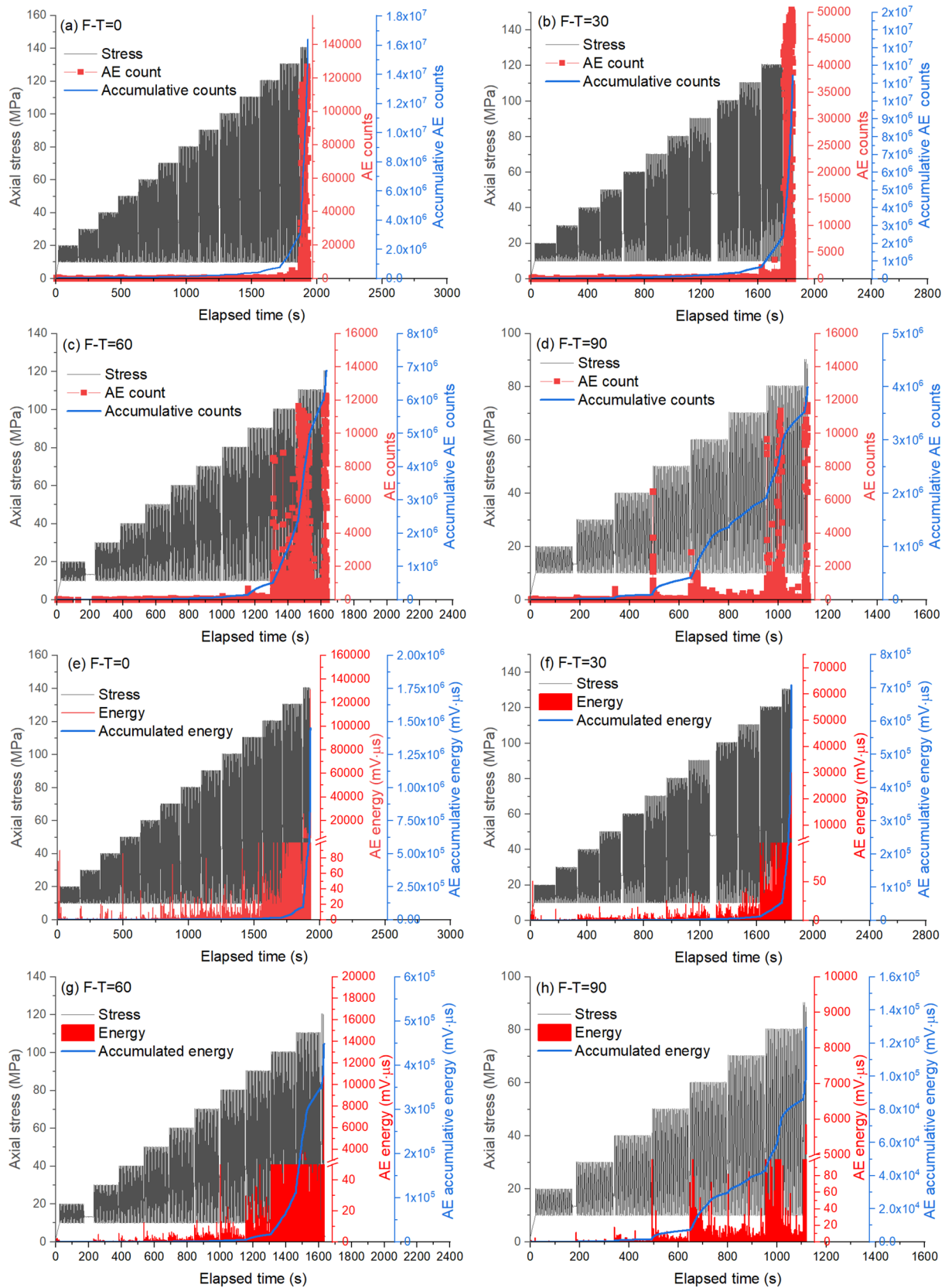
Fig. 12 Depiction of the the AE ring count/energy count evolution during rock deformation. (**a**–**d** Plots of the relationship between the AE ring count, accumulative AE ring count and experimental time; **e**–**h** plots of the relationship between the AE energy, accumulative AE enery and experimental time.)
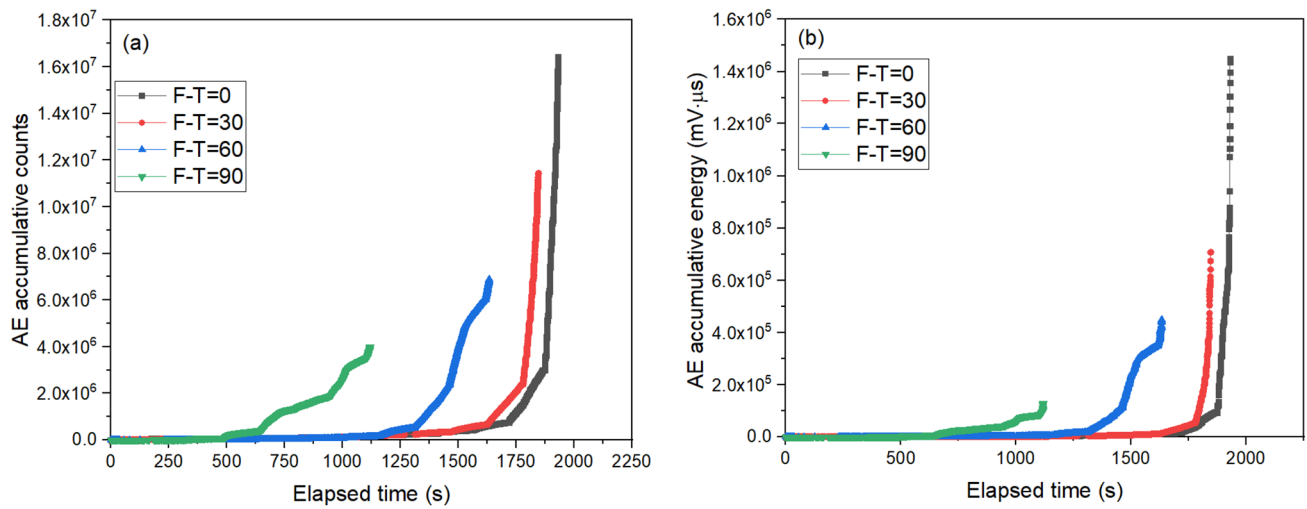
Fig. 13 Effect of the F–T treatment on AE activities. (**a** Plot of the influence of F–T cycle on AE accumulative counts; **b** plot of the influence of F–T cycle on AE accumulative energy.)
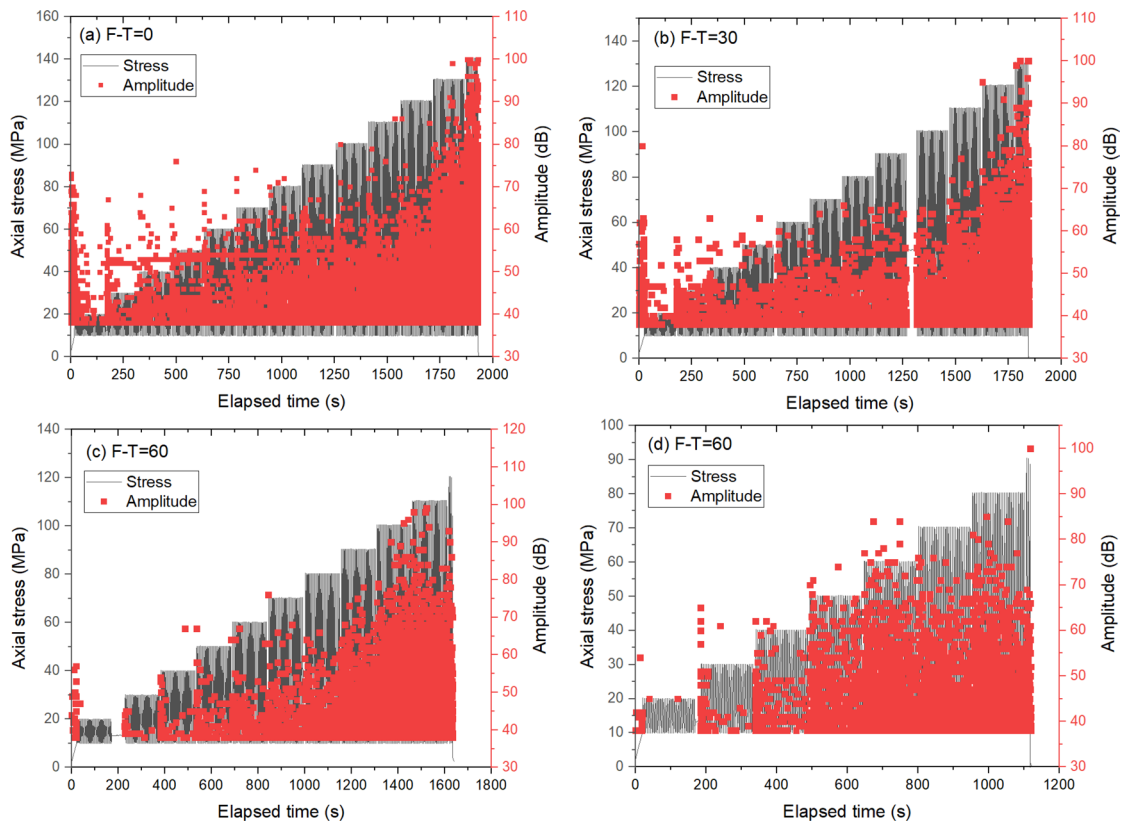

Fig. 14 Plots of the AE amplitude distribution, axial stress against loading time. (**a–d** The F–T cycle is 0, 30, 60, and 90, respectively.)

AE amplitude decreases with the increase of amplitude. The accumulative frequency curve also indicates that high-amplitude signals decrease with the loading time. The AE count distribution in Fig. 15 shows that proportion of the low-amplitude signals for rock experiencing 0 and 30 F–T cycles is more than the sample experiencing 60 and 90 F–T cycles. All the results imply that the energy released during rock fracture is relatively large for rock subjected to
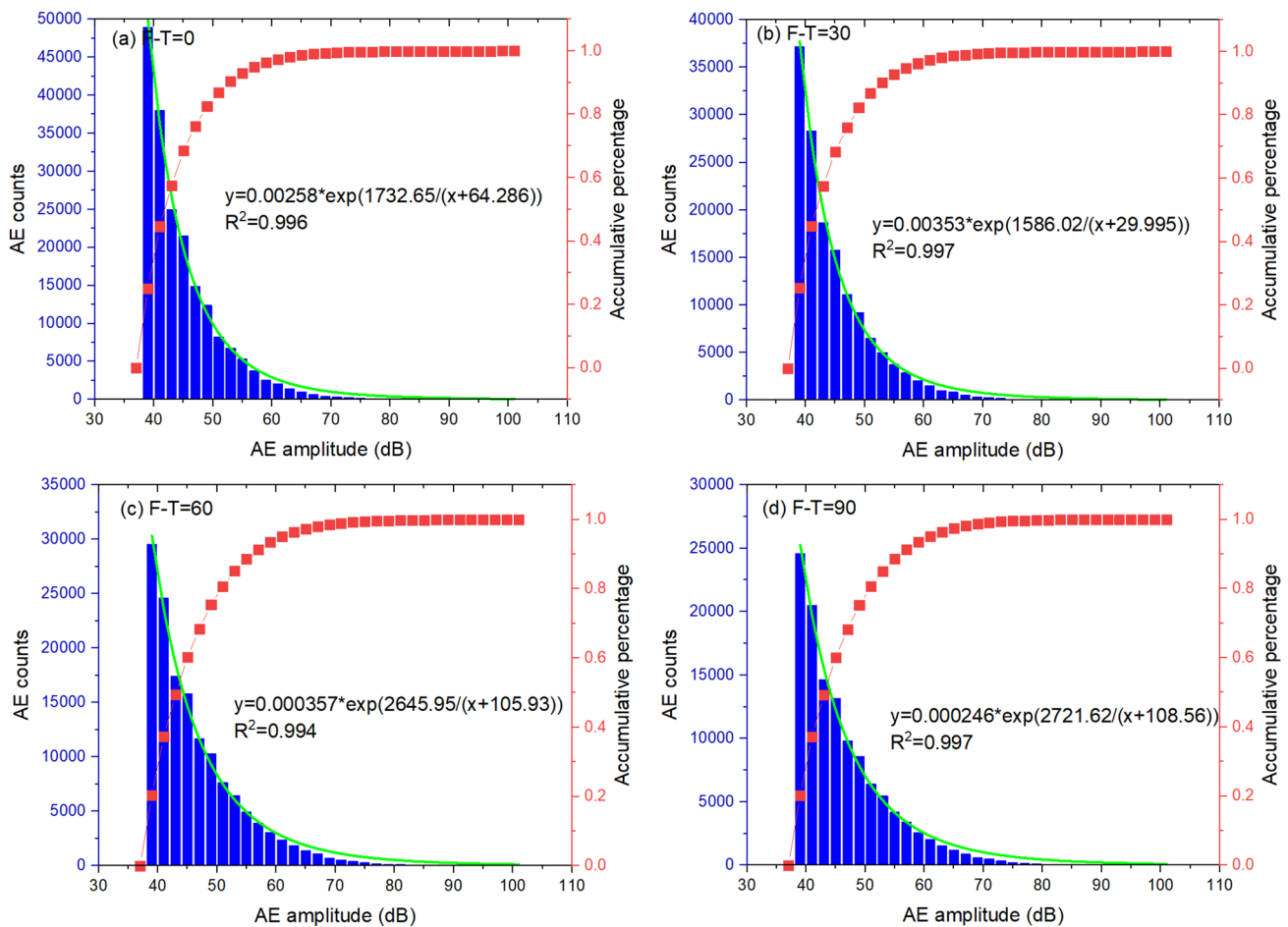
Fig. 15 Depiction of the evolution of AE b-value and volumetric strain with experimental time. (**a–d** The F–T cycle number is 0, 30, 60, and 90, respectively.)

fewer F–T treatments. To reveal the relationship between the AE amplitude and AE counts, an exponent fitting equation is employed to establish their link, and the correlation coefficient (R^2) is higher than 0.95, indicating a strong correlation.

To quantificationally describe the fracture and instability of the pre-flawed hollow-cylinder granite sample, the AE b-value is introduced herein. In tectonics, it has been shown that the AE b-value varies systematically for different modes of faulting (Ohnaka and Mogi 1982; Yang et al. 2020). The AE b-value is the frequency amplitude distribution obtained by using the Gutenberg–Richter relation commonly used in the seismic field (Dresen et al. 2020; Niu et al. 2020). The Gutenberg–Richter equation of acoustic emission is defined as follows:

$$\log_{10} N = a - b(A_{dB}/20), \tag{1}$$

where N is the frequency increment (i.e., the number of AE signals with amplitude greater than A_{dB}); the parameters "a"

and "b" are empirical constants obtained by linear curve fitting.

As the volumetric strain is a good parameter to describe rock instability, we plot the relationship between the AE b-value, volumetric strain, and the experimental time; see Fig. 16. Figure 16 compares the results of rock volumetric strain and AE b-value during rock failure. The AE b-value is calculated at the end of each cyclic-loading stage. The volumetric strain displays two patterns: one is that the first increases and then shows a decreasing trend, the inflection point corresponds to the dilatancy of rock, and it is the onset of rock instability; the other is the monotonous decreasing trend. The AE b-value displays a decreasing trend for all the test granite, and the decreasing rate becomes faster at high loading stage. The change of AE b-value with volumetric strain at various cyclic-loading stages is plotted in Fig. 16e. It shows that the AE b-value displays a positive correlation with the volumetric strain at the expansion stages. The decrease of AE b-value indicates that the damage degree becomes severe and instability gradually occurs. As a
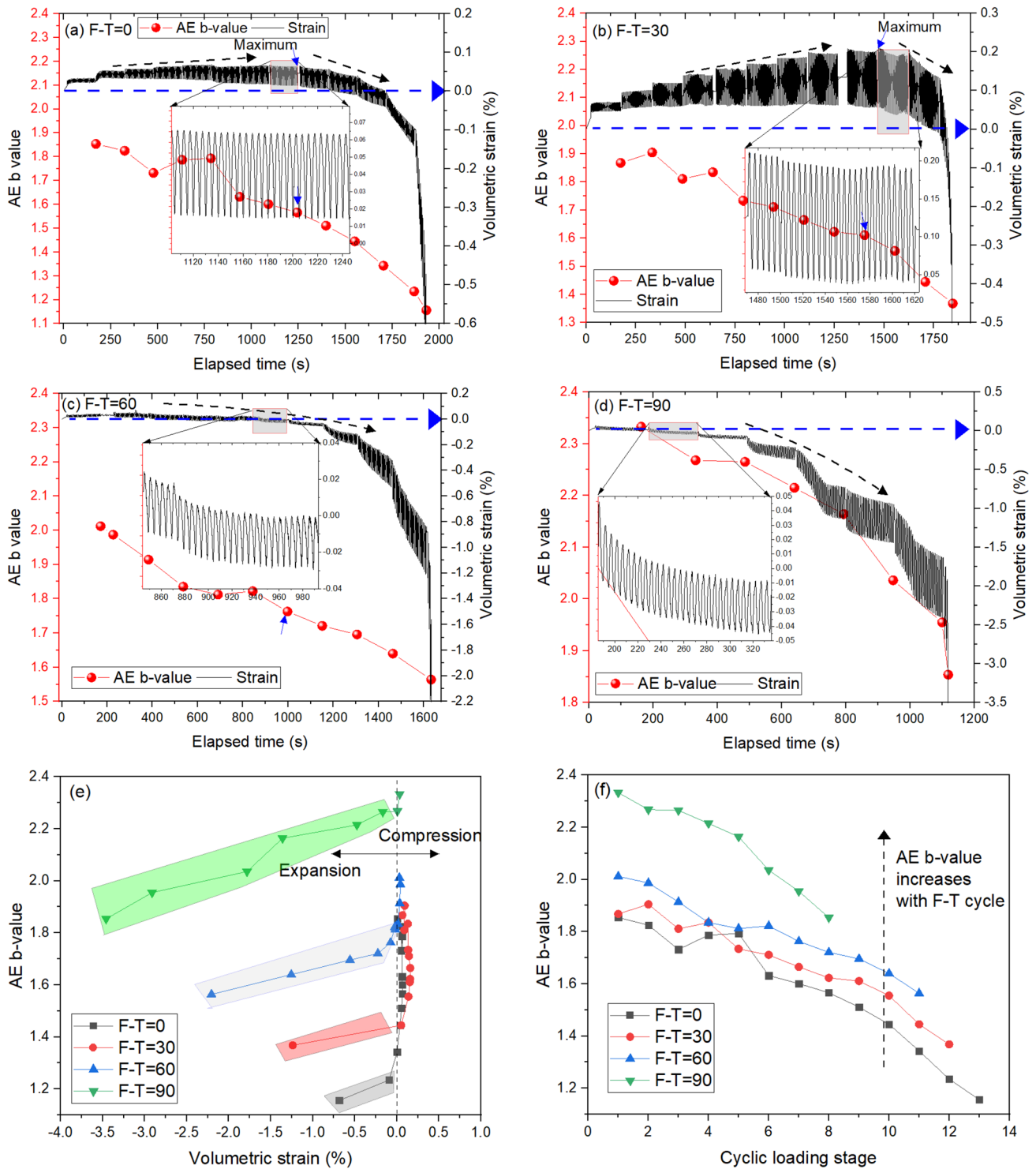
Fig. 16 Depiction of the evolution of AE *b*-value during rock deformation. (**a–d** Relationship between the volumetric strain, AE *b*-value and experimental time; **e** plots of the AE *b*-value against volumetric strain; **f** plot of the AE *b*-value against cyclic-loading stage.)

smaller AE b-value indicates a relatively large fracture of rock, the fracture is strong for rock without F–T treatment, as shown in Fig. 16f. For the sample having low b-value, it implies that the crack coalescence and hole spalling are

more severe than other cases. The fluctuation of the *b*-value indicates the complicated interactions between the fissures and hole, the crack propagation may be blocked at a certain
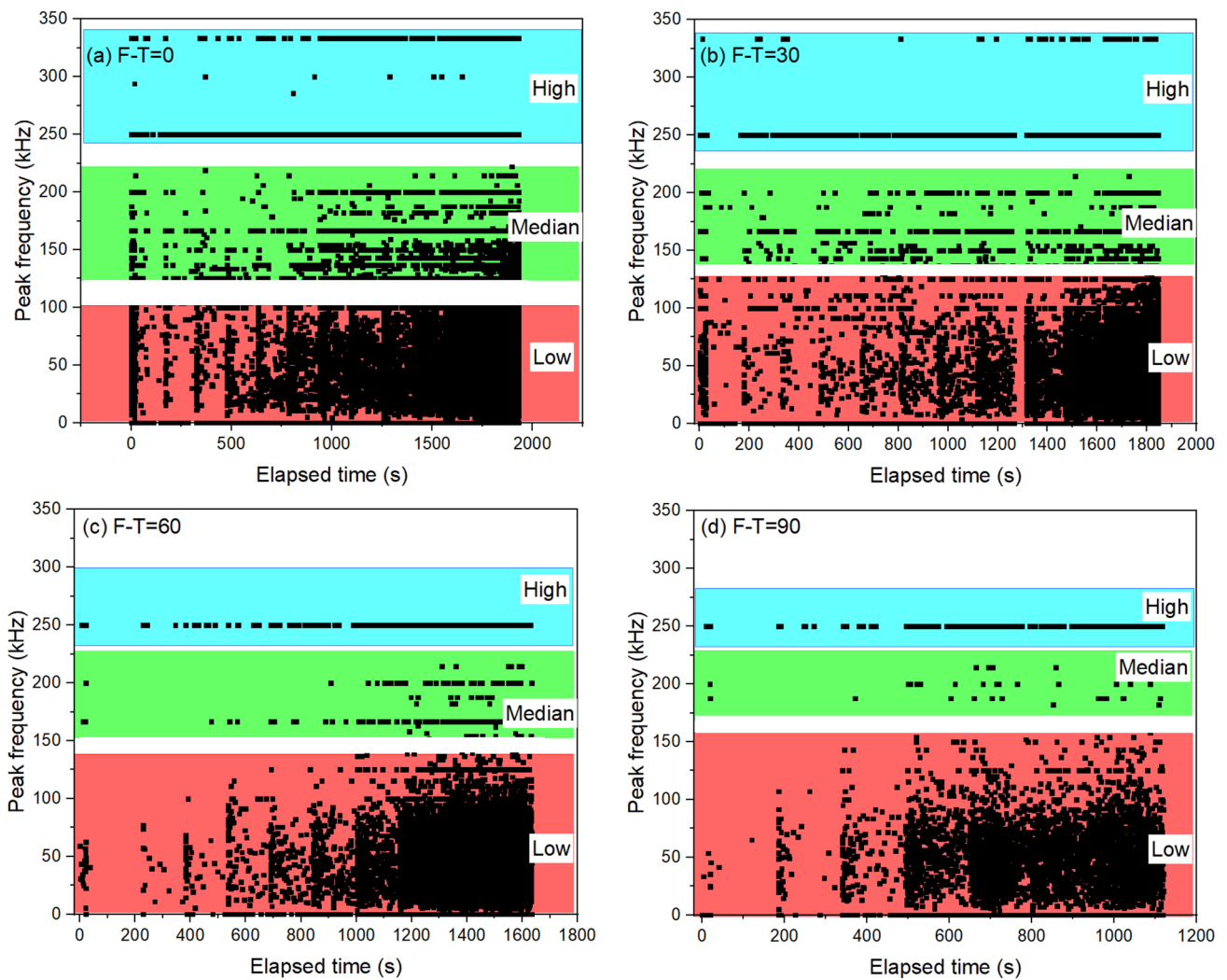
Fig. 17 Frequency spectrum analysis of the pre-flawed hollow-cylinder granite samples subjected to 0, 30, 60, and 90 F–T cycles

Table 2 Summarization of the frequency distribution for the tested hollow granite samples

F–T cycle	Low frequency (kHz)	Median frequency (kHz)	High frequency (kHz)
0	[0, 100]	[122, 224]	[242, 342]
30	[0, 127]	[138, 220]	[236, 338]
60	[0, 137]	[153, 225]	[231, 290]
90	[0, 156]	[174, 230]	[232, 282]

Table 3 Proportion of the low, median and high frequency during rock deformation

F–T cycle	Ratio of low frequency (%)	Ratio of median frequency (%)	Ratio of high frequency (%)
0	81.77	4.73	13.5
30	74.55	14.55	10.9
60	62.15	29.15	8.7
90	57.44	35.96	6.6

loading stage and the stored energy would release suddenly when the crack coalesces.

3.7 AE Spectral Frequency Analysis

Apart from the AE parameter (e.g., AE ring count, energy, amplitude) analysis to characterize rock fracturing during cyclic loads, the AE spectrum frequency analysis was carried out in this section. It is widely accepted that the acoustic emission signals consist of many different frequency components, and the cracking type, number, and size can be reflected from the waveform shape. In addition, the spectral (frequency) information reflects that the fracture process includes crack propagation and hole collapse, and the main

frequency of acoustic emission can better reflect the micro-cracks of rock and is more sensitive to acoustic emission counting (Muñoz-Ibáñez et al. 2021). The fast Fourier transform algorithm was employed to convert the discrete time domain signals into continuous frequency dominant signals. Figure 17 describes the main frequency distribution for the tested hollow-cylinder granite samples. It can be found that three distinct main frequency bands were divided for the tested granite samples. The main frequency intervals during the whole fracturing process are summarized in Table 2. The low-frequency interval is relatively smaller for the tested granite samples subjected to 0 and 30 F–T cycles compared to those of 60 and 90 F–T cycles.

To further clarify the influence of the previous freeze–thaw damage on the meso-damage mechanism of the hollow-cylinder rock, the proportion of these three kinds of signal is counted in Table 3. It is found that the proportion of low-frequency signals decreases and high-frequency signals also decrease with increasing F–T cycle. The results in Table 3 indicate that the large-scaled crack is prone to forming a sample having high F–T cycles. For rock with small F–T cycles, much more small-scaled cracks form and their number is larger than the rock with low flaw angle. The high-frequency AE signals correspond to fracturing-type signals, and their proportion decreases with increasing F–T cycle, indicating that high fracture energy is released for a rock sample subjected to relatively small F–T cycles.

3.8 Macro–Meso Failure Mechanism Analysis

To further reveal the impact of freeze–thaw damage on crack coalescence and hole collapse for the hollow-cylinder granite, post-test CT scanning was conducted for the rock samples. A total of three slices were obtained for rock samples experiencing 0, 30, 60, and 90 F–T cycles, respectively. The

crack pattern and hole shape inside the deformed sample can be clearly detected in Fig. 18. According to the basic principle of X-ray CT, flaws, as a low-density structure, present as gray or black color (Karpyn et al. 2009; Wang et al. 2022a, b, c). A series of digital image process methods were employed to extract the crack from the CT slice. It is found that the crack density decreases with F–T cycles. It is a maximum and minimum for the sample subjected to 0 and 90 F–T cycles. Influenced by the pre-existing flaws, failure of the hollow-cylinder granite is the combination of crack coalescence with hole collapse. The crack propagation paths are blocked by the rock bridge, and the hollow hole spalls at the intersection part of crack and hole. The collapse degree of the hole is also impacted by the freeze–thaw number and is the largest for a sample without F–T treatment. The CT images show that the newly formed crack distributes inhomogeneously, and the cracks are concentrated at a side having a pre-existing flaw. Although the pre-existing flaw has the same shape and orientation, their propagation path is different and impacted by the previous freeze–thaw damage.

The plastic wrapped around the granite samples was removed after the CT scanning. We observed the crack morphology on the rock surface visually, as shown in Fig. 19. Although the existence of the two fissures alters the propagation path of the cracks, the cracks propagate parallel or subparallel to the loading direction. This is to say, the local propagation path at the fissure tip is influenced by the fissure orientation. The crack on the rock surface shows that its density is different and impacted by the freeze–thaw damage. The crack density is the largest for the sample without F–T treatment, and it is the smallest for the rock having 90 F–T cycles. The failure morphology shows that the two fissures communicate with each other and cross the hollow hole. According to the macroscopic failure morphology of the
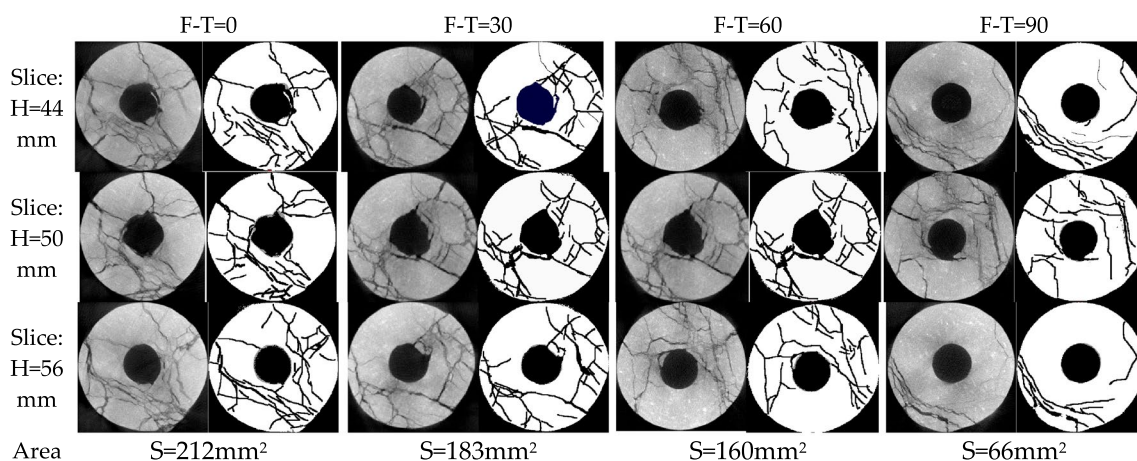

Fig. 18 Reconstruction of the CT images at the rock bridge segment for the pre-flawed hollow-cylinder granite experiencing 0, 30, 60, and 90 F–T cycles
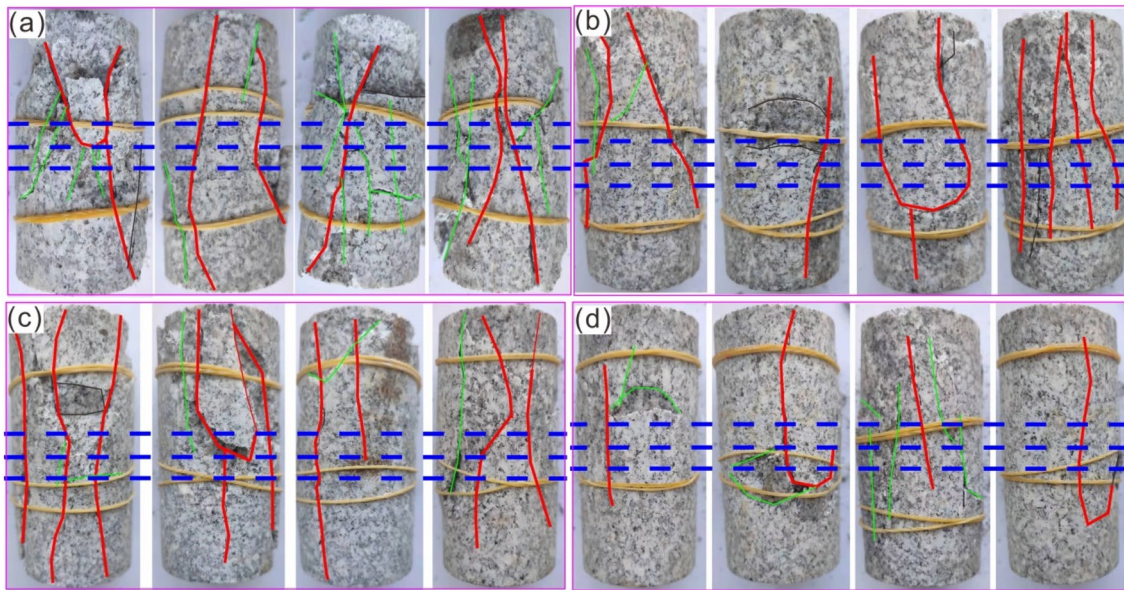
Fig. 19 Morphology of the pre-flawed granite samples containing two fissures. The red line indicates the main crack, green line indicates the secondary crack and blue line indicates the CT scanning positions. (**a–d** The F–T cycle is 0, 30, 60, and 90, respectively.)

tested rock, it is found that the splitting failure mode is for all the tested rock.

4 Conclusions

Multistage cyclic-loading testing was conducted on freeze-thawed hollow-cylinder granite containing two fissures. The influences of the previous freeze–thaw damage on rock microstructure, strength, deformation, stiffness, AE activities, and failure morphology were systematically investigated. According to the analysis above, some key conclusions are summarized below:

(1) Irreversible damage caused by freeze–thaw increases with the increase of the F–T cycle. The microstructure in the rock matrix is different and is displayed as the occurrences of large pore, super large pore and microcracks as the F–T number grows.
(2) The rock stiffness described by the secant modulus and Poisson's ratio is impacted by the F–T cycle. The secant modulus decreases and Poisson's ratio increases with the increase of the F–T cycle, and their changing rate becomes faster near rock failure.
(3) The previous freeze–thaw damage influences the AE ring count, energy count, amplitude distribution, and spectral pattern. Large fracture signals are captured

for rock that has smaller F–T cycles and at the stress-increasing moment. The AE b-value is consistent with the volumetric strain and decreases rapidly near rock failure. A large-scaled crack is prone to form for a sample having high F–T cycles; however, the proportion of high-frequency AE signals that correspond to fracturing-type signals decreases with increasing F–T cycle.
(4) The macroscopic and mesoscopic failure morphology analysis reveals the interactions between the two fissures and hollow hole. It is found that a complex network is prone to be formed for a rock subjected to a smaller F–T cycle, and its fracture degree is high. The crack coalescence and hole collapse patterns and the associated structural deterioration of the rock bridge segment are obviously influenced by the F–T treatment.

Data Availability The experimental data used to support the findings of this study are included within the article.

Declarations

Conflict of Interest The authors declare no conflict of interest.

References

ASTM (2007) Standard test method for compressive strength and elastic moduli of intact rock core specimens under varying states of stress and temperatures. Annual book of ASTM standards

Alsayed MI (2002) Utilising the Hoek triaxial cell for multiaxial testing of hollow rock cylinders. Int J Rock Mech Min Sci 39(3):355–366

Bagde MN, Petroš V (2005) Fatigue properties of intact sandstone samples subjected to dynamic uniaxial cyclical loading. Int J Rock Mech Min 42:237–250

Cerfontaine B, Collin F (2018) Cyclic and fatigue behaviour of rock materials: review, interpretation and research perspectives. Rock Mech Rock Eng 51(2):391–414

Dresen G, Kwiatek G, Goebel T, Ben-Zion Y (2020) Seismic and aseismic preparatory processes before large stick–slip failure. Pure Appl Geophys 177(12):5741–5760

Forte G, Verrucci L, Di Giulio A, De Falco M, Tommasi P, Lanzo G, Santo A (2021) Analysis of major rock slides that occurred during the 2016–2017 Central Italy seismic sequence. Eng Geol 290:106194

Ghobadi MH, Babazadeh R (2015) Experimental studies on the effects of cyclic freezing–thawing, salt crystallization, and thermal shock on the physical and mechanical characteristics of selected sandstones. Rock Mech Rock Eng 48:1001–1016

Huang SB, Liu QS, Cheng AP, Liu YZ, Liu GF (2018) A fully coupled thermo-hydro-mechanical model including the determination of coupling parameters for freezing rock. Int J Rock Mech Min Sci 103:205–214

Karpyn ZT, Alajmi A, Radaelli F, Halleck PM, Grader AS (2009) X-ray CT and hydraulic evidence for a relationship between fracture conductivity and adjacent matrix porosity. Eng Geol 103(3–4):139–145

Kong LW, Zeng ZX, Bai W, Wang M (2018) Engineering geological properties of weathered swelling mudstones and their effects on the landslides occurrence in the Yanji section of the Jilin-Hunchun high-speed railway. Bull Eng Geol Env 77(4):1491–1503

Lee DH, Juang CH, Chen JW, Lin HM, Shieh WH (1999) Stress paths and mechanical behavior of a sandstone in hollow cylinder tests. Int J Rock Mech Min Sci 36(7):857–870

Li G, Cheng X, Hu L, Tang C (2021a) The material-structure duality of rock mass: Insight from numerical modeling. Int J Rock Mech Min Sci 144:104821

Li Y, Zhai Y, Meng F, Zhang Y (2021b) Study on the influence of freeze-thaw weathering on the mechanical properties of Huashan granite strength. Rock Mech Rock Eng. https://doi.org/10.1007/s00603-021-02497-w

Lu YN, Li XP, Chan A (2019) Damage constitutive model of single flaw sandstone under freeze–thaw and load. Cold Reg Sci Technol 159:20–28

Masoumi H, Saydam S, Hagan PC (2015) A modification to radial strain calculation in rock testing. Geotech Test J 38(6):813–822

Mateos RM, García-Moreno I, Azañón JM (2012) Freeze–thaw cycles and rainfall as triggering factors of mass movements in a warm Mediterranean region: the case of the Tramuntana Range (Majorca, Spain). Landslides 9(3):417–432

Miao S, Pan PZ, Li S, Chen J, Konicek P (2021) Quantitative fracture analysis of hard rock containing double infilling flaws with a novel DIC-based method. Eng Fract Mech. https://doi.org/10.1016/j.engfracmech.2021.107846

Mogi K (1981) Earthquake prediction program in Japan. In: Simpson DW, Richards PG (eds) Earthquake prediction: an international review, vol 4. AGU, Washington, DC, pp 635–666

Muñoz-Ibáñez A, Delgado-Martín J, Herbón-Penabad M, Alvarellos-Iglesias J (2021) Acoustic emission monitoring of mode I fracture toughness tests on sandstone rocks. J Pet Sci Eng 205:108906

Nicholson DT, Nicholson FH (2000) Physical deterioration of sedimentary rocks subjected to experimental freeze–thaw weathering. Earth Surf Proc Land 25(12):1295–1307

Niu Y, Zhou XP, Zhou LS (2020) Fracture damage prediction in fissured red sandstone under uniaxial compression: acoustic emission b-value analysis. Fatigue Fract Eng Mater Struct 43(1):175–190

Ohnaka M, Mogi K (1982) Frequency characteristics of acoustic emission in rocks under uniaxial compression and its relation to the fracturing process to failure. J Geophys Res Solid Earth 87(B5):3873–3884

Scholz CH (1968) Microfracturing and the inelastic deformation of rock in compression. J Geophys Res 73:1417–1432

Wang Y, Zhang B, Li B, Li CH (2021a) A strain-based fatigue damage model for naturally fractured marble subjected to freeze-thaw and uniaxial cyclic loads. Int J Damage Mech 30(10):1594–1616

Wang Y, Feng WK, Hu RL, Li CH (2021b) Fracture evolution and energy characteristics during marble failure under triaxial fatigue cyclic and confining pressure unloading (FC-CPU) conditions. Rock Mech Rock Eng 54(2):799–818

Wang Y, Han JQ, Song ZY, Zhu C (2021c) Macro–meso failure behavior of pre-flawed hollow-cylinder granite under multi-level cyclic loads: insights from acoustic emission and post-test CT scanning. Eng Fract Mech 258:108074

Wang Y, Zhu C, Song ZY, Gong S (2022a) Macro–meso failure characteristics of circular cavity-contained granite under unconventional cyclic loads: a lab-scale testing. Measurement 188:110608

Wang Y, Yang HN, Han JQ, Zhu C (2022b) Effect of rock bridge length on fracture and damage modelling in granite containing hole and fissures under cyclic uniaxial increasing-amplitude decreasing-frequency (CUIADF) loads. Int J Fatigue. https://doi.org/10.1016/j.ijfatigue.2022.106741

Wang Y, Cao Z, Song Z, Zhu C, Han J (2022c) On fracture and damage evolution modelling of fissure-hole containing granite induced by multistage constant-amplitude variable-frequency cyclic loads. Fatigue Fract Eng Mater Struct. https://doi.org/10.1111/ffe.13663

Xu J, Liu Y, Ni Y (2019) Hierarchically weighted rough-set genetic algorithm of rock slope stability analysis in the freeze–thaw mountains. Environ Earth Sci 78(6):1–14

Yang SQ (2018) Fracturing mechanism of compressed hollow-cylinder sandstone evaluated by X-ray micro-CT scanning. Rock Mech Rock Eng 51(7):2033–2053

Yang J, Mu ZL, Yang SQ (2020) Experimental study of acoustic emission multi-parameter information characterizing rock crack development. Eng Fract Mech 232:107045

Zhou JW, Cui P, Hao MH (2016) Comprehensive analyses of the initiation and entrainment processes of the 2000 Yigong catastrophic landslide in Tibet. China Landslides 13(1):39–54

Zhou XP, Niu Y, Zhang JZ, Shen XC, Zheng Y, Berto F (2019) Experimental study on effects of freeze-thaw fatigue damage on the cracking behaviors of sandstone containing two unparallel fissures. Fatigue Fract Eng Mater Struct 42(6):1322–1340